PHYSICAL REVIEW D **91,** 116010 (2015)

Magnetic catalysis and inverse magnetic catalysis in QCD

Niklas Mueller[1] and Jan M. Pawlowski[1,2]

[1]*Institut für Theoretische Physik, Universität Heidelberg, Philosophenweg 16, 69120 Heidelberg, Germany*

[2]*ExtreMe Matter Institute EMMI, GSI Helmholtzzentrum für Schwerionenforschung mbH, Planckstraße 1, D-64291 Darmstadt, Germany*

(Received 19 March 2015; published 22 June 2015)

We investigate the effects of strong magnetic fields on the QCD phase structure at vanishing density by solving the gluon and quark gap equations, and by studying the dynamics of the quark scattering with the four-Fermi coupling. The chiral crossover temperature as well as the chiral condensate are computed. For asymptotically large magnetic fields we find magnetic catalysis, while we find inverse magnetic catalysis for intermediate magnetic fields. Moreover, for large magnetic fields the chiral phase transition for massless quarks turns into a crossover. The underlying mechanisms are then investigated analytically within a few simplifications of the full numerical analysis. We find that a combination of gluon screening effects and the weakening of the strong coupling is responsible for the phenomenon of inverse catalysis. In turn, the magnetic catalysis for large magnetic fields is already indicated by simple arguments based on dimensionality.

DOI: 10.1103/PhysRevD.91.116010 PACS numbers: 11.15.Tk, 11.30.Rd, 12.38.Aw, 12.38.Gc

I. INTRODUCTION

In recent years there has been a growing interest in the QCD phase structure in the presence of strong magnetic fields; see e.g. Refs. [1–8]. Such fields may play an important role for the physics of the early Universe, in compact stars, and in noncentral heavy ion collisions [4,7,9,10].

Despite the rich phenomenology, theoretical predictions are challenging. Starting from QED, e.g. Refs. [11–14], the influence of magnetic fields on QCD was investigated in model calculations, e.g. Refs. [15–29], such as quark-meson, Nambu–Jona-Lasinio models and AdS/QCD, e.g. Refs. [30–36]; with functional renormalization group (FRG) methods, e.g. Refs. [37–43]; Dyson-Schwinger (DSE) equations, e.g. Refs. [6,44–46]; and in lattice calculations, e.g. Refs. [47–53].

The importance of magnetic fields for chiral symmetry breaking has been pointed out in Ref. [11]. It has been argued that chiral symmetry breaking is enhanced due to an effective dimensional reduction, the *magnetic catalysis*. This effect has been linked to an increase of the chiral condensate as well as that of the critical temperature T_c in model studies. Recent lattice results, Refs. [47–49,53], have shown that while the chiral condensate indeed is increased, the critical temperature decreases with an increasing magnetic field, at least for small enough magnetic field strength. This effect has been called *inverse magnetic catalysis* or *magnetic inhibition* [54].

Continuum studies have mainly been performed in low-energy fermionic models, such as the (Polyakov-loop-enhanced) quark-meson or NJL model. Hence, the reason for the discrepancy has to relate to the full dynamics of QCD, and in particular the backreaction of the matter sector to the gluonic fluctuations. There have been a number of improvements to these model studies to include QCD dynamics [24,26–28,55,56]. Input parameters of low-energy effective models, such as the four-Fermi coupling, should be determined from the QCD dynamics at larger scales. At these scales they are sensitive to sufficiently large external parameters such as temperature, density, or magnetic fields. This has been emphasized and used in functional FRG studies; see Refs. [57–60]. The dependence of the four-Fermi coupling on temperature and magnetic field effects including gluon screening has been investigated in the recent FRG work [43] of QCD in strong magnetic fields, where inverse magnetic catalysis with small magnetic fields and a *delayed magnetic catalysis* with large fields was found; see also Ref. [36] for an AdS/QCD computation.

In the present work we investigate (inverse) magnetic catalysis by solving the coupled quark and gluon gap equations within the DSE approach to QCD, and within a FRG study of the four-Fermi coupling based on QCD flows and low-energy effective models. We find magnetic catalysis with large magnetic fields, while inverse magnetic catalysis takes place with small magnetic fields.

The present work is organized as follows: The gap equations for quark and gluon propagators at finite temperature and magnetic field in two-flavor QCD are discussed in Sec. II. We discuss the dependence of the chiral transition temperature T_c on the magnetic field as well as the magnetic field dependence of the chiral condensate. In Sec. III, the mechanisms behind the phenomena of magnetic and inverse magnetic catalysis are evaluated within analytically accessible approximations to the gap equations as well as to the dynamics of the four-Fermi coupling. In this setup we are also able to reproduce the lattice results at $eB < 1\ \mathrm{GeV}^2$. In summary, this provides a complete picture of chiral symmetry breaking in the presence of magnetic fields in QCD.

II. CHIRAL SYMMETRY BREAKING IN LARGE MAGNETIC FIELDS

We investigate chiral symmetry breaking in the presence of large magnetic fields within a functional continuum approach. To this end we calculate the chiral condensate for the two lightest quark flavors and obtain the critical temperature T_c at finite magnetic field. This is done by solving the gap equations for the quark and gluon propagator in the presence of a magnetic field using the Ritus method [61–67]. The computations are performed in the Landau gauge.

A. Quark and gluon gap equations

The gap equation for the quark propagator, see Fig. 1, depends on the gluon propagator and the quark-gluon vertex. The former is expanded about the quenched propagator. This expansion has been successfully used at vanishing temperature, e.g. Refs. [68,69], and at finite temperature, e.g. Refs. [70–73]; the reliability of this expansion has been discussed in Ref. [74]. The quark-gluon vertex is estimated with the help of Slavnov-Taylor identities from the quark and gluon propagators. The systematic error of the latter estimate gives rise to the dominating systematic error; at vanishing temperature this has been investigated in Ref. [75], and a related upgrade of the vertex will be used in a subsequent work.

The inverse quark and gluon propagators, $G_q(q)$ and $G_A(q)$, respectively, read in a tensor decomposition at finite eB and T

$$G_q^{-1}(q) = Z_q(q)(i\gamma_3 q_3 + i\gamma_0 q_0 Z_0 + i\gamma_\perp q_\perp Z_\perp + M),$$
$$G_A^{-1\mu\nu}(q) = (Z_\parallel P_\parallel^{\mu\nu} + Z_\perp P_\perp^{\mu\nu})q^2 + \frac{1}{\xi}\frac{q^\mu q^\nu}{q^2}, \tag{1}$$

where the quark propagator is given in the Ritus spectral representation [66,67], which is discussed e.g. in Refs. [6,61,76]. The fermion propagator in position space is then given as

$$G_q(x,y) = \sum\!\!\!\!\!\!\int_p E_p(x) G_q(p) \bar{E}_p(y), \tag{2}$$

with the sum/integral over the Ritus/Matsubara eigenvalues. The eigenfunctions $E_p(x)$, which form a complete orthonormal basis, are given explicitly in Ref. [6]. We note that the propagator is not translation invariant, $G_q(x,y) \neq G_q(x-y)$, as the eigenfunctions induce a nontrivial position dependence. In Eq. (1), $P_\parallel^{\mu\nu} = (g_\parallel^{\mu\nu} - p_\parallel^\mu p_\parallel^\nu / p_\parallel^2)$ and $P_\perp = P - P_\parallel$, where $P_{\mu\nu}$ is the transverse projector. The projection operator $g_\parallel^{\mu\nu}$ has the property $g_\parallel^{\mu\nu} p_\parallel^\mu = p_\parallel^\nu$. The Ritus representation in Eq. (1) for the quark propagator is equivalent to the Schwinger proper time method; see e.g. Ref. [77]. The important difference, however, is that the Schwinger proper time method utilizes a Fourier decomposition of the propagator times a phase accounting for nontranslational invariance, which in the case of the Ritus propagator is encoded in the eigenfunctions in position representation.

In the following, we will denote $Z_A \equiv Z_\parallel$ and concentrate on the Landau gauge, $\xi = 0$. The STI-induced parametrization of the quark-gluon vertex is introduced as

$$\Gamma^\mu(q,p) = \gamma^\mu z_{\bar{q}Aq}^{\mathrm{DSE}}(q,p), \tag{3}$$

with $z_{\bar{q}Aq}^{\mathrm{DSE}}(q,p)$ discussed in Appendix A. The quark gap equation can be written in a compact notation as

$$G_q^{-1}(p) = G_{q,0}^{-1}(p) + C_f \sum\!\!\!\!\!\!\int_q (g\gamma^\mu) G_q(q) \Gamma^\nu(q,p) G_A^{\mu\nu}(q'), \tag{4}$$

with $q' = q - p$ and $G_{q,0}$ as the bare propagator. The integration $\sum\!\!\!\!\!\!\int_q$ stands for an integration over momenta, as well as sums over Matsubara frequencies and Landau levels. The gluon propagator can be expanded about its pure glue part,

$$G_A^{-1\mu\nu}(p) = G_{\mathrm{glue}}^{-1\mu\nu}(p) + \Pi_f^{\mu\nu}(p), \tag{5}$$

where we have written the fermionic part of the gluon self-energy explicitly, while the gluon and ghost loop contributions are contained in G_{glue}. The corresponding DSE for the gluon propagator within this expansion is depicted in Fig. 2. In the following, we consider the backreaction of the

FIG. 1. Quark DSE equation. Lines with blobs stand for fully dressed propagators, and vertices with large blobs stand for fully dressed vertices. Lines without blobs stand for classical propagators, and vertices with small blobs stand for classical vertices.

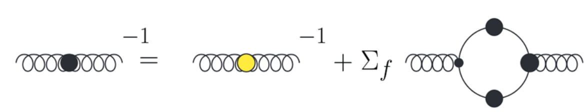

FIG. 2 (color online). Gluon DSE equation. The gluon line with the yellow dot represents the pure glue loops.

vacuum polarization on the pure glue part as small, and approximate

$$G^{-1\mu\nu}_{\rm glue}(p) \approx G^{-1\mu\nu}_{\rm YM}(p). \tag{6}$$

At vanishing temperature, this has been shown to hold quantitatively for momenta $q \gtrsim 4$ GeV, while for smaller momenta this approximation still holds qualitatively with an error of less than 20%; see Fig. 6 in Ref. [74]. Note that for momenta $q \gtrsim 4$ GeV the dominant effect of the unquenching is the modification of the scales ($\Lambda_{\rm YM} \to \Lambda_{\rm QCD}$) and the momentum dependence induced by the different β functions. This is well captured with the above procedure. In turn, at lower momentum scales the nonperturbative mass gap related to confinement comes into play. The magnetic field leads to a shift in the momentum dependence such as that of the running coupling, as well as (additional) mass gaps in propagators. For both asymptotic regimes ($eB \to 0$ and $eB \to \infty$), these effects are well captured semiperturbatively, and we expect that the approximation (6) holds well. For the intermediate regime, we rely on the error estimate at zero temperature of about 20% deduced from Ref. [74].

The fermionic vacuum polarization part $\Pi^{\mu\nu}_f(P)$ reads

$$\Pi^{\mu\nu}_f(p) = \frac{1}{2}\mathrm{tr}\sum\!\!\!\!\!\!\!\int_q (g\gamma^\mu) G_q(q)\Gamma^\nu(q,p)G_q(q'), \tag{7}$$

where the trace includes a sum over the quark flavors. Details of this expansion can be found in Ref. [6]. Here we proceed in the lowest Landau-level approximation, where we write down the most general tensor decomposition for gluon and quark propagators. Projecting onto different tensor compositions, we obtain a coupled set of equations for the dressing functions of the different tensor components. In the next section, we will comment on the relation of the DSE equations to other functional expansions and discuss the numerical solutions to these equations.

B. Skeleton expansion

Before proceeding to the numerical analysis, we discuss the standard approximation schemes for the quark-gluon vertex used in the DSE framework from a more general point of view. This allows us to connect the present ansatz to the approximations used in gap equations derived within other functional approaches, such as the FRG or nPI approaches.

DSE studies have made extensive use of the specific input for the quark-gluon vertex and the YM-gluon propagator in (A2) and (A4) and similar truncations with great success. Since the quark and gluon self-energy diagrams, depicted in Figs. 1 and 2, contain one bare vertex, the correct renormalization group behavior and momentum dependence of the equations must be discussed carefully. The truncations to the gap equations (4) and (5) can actually be very well motivated from a skeleton expansion of the 1PI effective action, which would yield similar diagrams as in Figs. 1 and 2, but with both vertices dressed. Figure 3 serves to strengthen this motivation as it becomes clear that all approximations should encode the correct behavior of the four-Fermi interaction, which is at the heart of chiral symmetry breaking. This allows us to consistently reshuffle functional dependencies in the interaction kernels of the above equations.

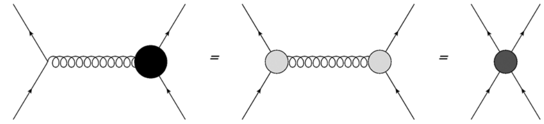

FIG. 3. Relation of the quark DSE interaction kernel to a 1PI skeleton expansion, which in effect induces an effective momentum-dependent four-Fermi vertex.

In turn, the FRG approach (or nPI effective action) can be used to systematically derive gap equations in terms of full propagators and vertices, respectively; see e.g. Ref. [78]. Here, we simply note that the 1PI effective action can be written as

$$\Gamma[\phi] = \frac{1}{2}\mathrm{Tr}\ln\Gamma[\phi] + \int_t \partial_t\Gamma_k[\phi] - \text{terms}, \tag{8}$$

where ϕ encodes all species of fields, the trace in (8) sums over momenta, internal indices and all species of fields include relative minus signs for fermions (ψ and $\psi^\dagger$ are counted separately), and a logarithmic RG scale $t = \ln k$. The RG scale in (8) is an infrared scale. Momenta $p^2 \lesssim k^2$ are suppressed in $\Gamma_k[\phi]$, and $\Gamma[\phi] = \Gamma_{k=0}[\phi]$. The second term on the right-hand side of (8) is a RG improvement term which only contains diagrams with two loops and more in full propagators and vertices. To see this, we discuss the gap equation derived from (8). It follows by taking the second derivative of (8) with respect to the fields. The first term of the right-hand side gives the diagrams as in Fig. 1 and Fig. 2 with only full vertices (and additional tadpole diagrams). These diagrams can be iteratively reinserted into the RG improvement term, systematically leading to higher loop diagrams in full propagators and vertices. Due to its sole dependence on dressed correlation functions, such a diagrammatics naturally encodes the momentum—as well as the RG—running on an equal footing. This also facilitates the consistent renormalization. Note, however, that it comes at the price of an infinite series of loop diagrams which can be computed systematically. Here we take the simplest nontrivial approximation, which boils down to Figs. 1 and 2 with only full vertices. In terms of the original gap equation, this leads to the relation

$$z^{\rm DSE}_{\bar{q}Aq} \approx (z^{\rm 1PI}_{\bar{q}Aq})^2, \tag{9}$$

where $z^{1PI}_{\bar{q}Aq}$ is the dressing function of the 1PI quark-gluon vertex. This immediately leads to the standard DSE dressing in (A2). Moreover, in our numerical study, the vertices are evaluated at their symmetric momentum point.

Note that, while the ansatz for $z^{DSE}_{\bar{q}gq}$ is indeed consistent when used in the quark and gluon gap equations, it cannot be used in functional equations for higher vertices such as the four-Fermi vertex. It is already clear from the discussion above that a consistent evaluation of renormalization group running and momentum dependence must be considered separately for each vertex equation.

C. Results

We numerically solve the coupled system of quark and gluon functional equations in the lowest Landau-level approximation at finite temperature. This approximation is valid in the presence of a clear scale hierarchy with $eB \gg \Lambda_{\mathrm{QCD}}$. We use an ansatz for Γ^μ similar to that used in DSE studies, e.g. Refs. [6,79], discussed in Appendix A, but adapted for temperature and magnetic field effects.

While at large momentum the influence of temperature and magnetic fields is very small, at large temperature and magnetic field the system is effectively dimensionally reduced, and hence the momentum dependencies corresponding to the absent dimensions vanish. This can be accounted for if we replace $Q_\perp^2$ with $2|eB|$ once $Q_\perp^2 < 2|eB|$, and Q_0 with $2\pi T$ for $Q_0 < 2\pi T$ as the relevant scale in the quark gluon vertex, which is consistent with renormalization group arguments. Within this parametrization we are still left to decide what exact momentum scale to choose, at which the influence of the external scales T and eB is small already. We investigate this question in detail in Sec. III A.

The gluon propagator deserves some additional attention. It is decomposed into different polarization components in the presence of an external magnetic field; see e.g. Ref. [6]. Apart from the splitting into longitudinal and transverse components with respect to the heat bath, there is an additional splitting transverse and longitudinal to the magnetic field. In the lowest Landau-level approximation only the polarization subspace projected onto by $P_\parallel^{\mu\nu} = (g_\parallel^{\mu\nu} - p_\parallel^\mu p_\parallel^\nu / p_\parallel^2)$ receives contributions from the quark loop in the self-energy; see Ref. [6]. Note that in analogy to temperature effects, the other gluon components must also receive contributions from the interaction with the magnetic field, as gluon and ghost loops mix different polarization components. This is an important difference between QCD and QED. From dimensionality these contributions are linear in eB at least for asymptotically large magnetic fields, leaving aside implicit B dependencies via the vertices. Their full computation is beyond the scope of the present work. Here we investigate the following two limiting cases:

(1) *Scenario 1:* We simply neglect the screening effect of the magnetic field on those polarization components that feel magnetic effects only through the Yang-Mills sector in a QED-type approximation. This leads to underestimating the effects leading to inverse magnetic catalysis, and hence an upper limit for T_c.

(2) *Scenario 2:* For the large magnetic fields discussed here, the gluon and ghost loop contributions to the self-energy must have a similar dependence on eB to the fermionic part. Since this sector does not directly contain charged particles, the effect of the magnetic field on the YM sector is suppressed by powers of the involved couplings. Hence, most likely the B dependence is much smaller than that from the fermionic sector. As a limiting case we will assume the same magnitude of the self-energy for all gluon components, which is given by the fermionic contributions. With that, we overestimate the gluon screening effect and obtain a lower limit for T_c.

Both scenarios give consistent limiting cases for the truncation used here.

As an order parameter for chiral symmetry breaking, we calculate the chiral condensate as a function of temperature and magnetic field in two-flavor QCD in the limit of vanishing bare quark masses $m_u \approx m_d \approx 0$. The Ritus method is not reliable for rather small values of $q_f eB$, with $q_f + 2/3$ and $-1/3$ for up and down quarks, respectively. We expect the lowest Landau-level approximation to be a good estimate once $eB \gtrsim 4\ \mathrm{GeV}^2$ (see Ref. [6]), which is also the regime where the approximation (6) works well for vanishing temperature.

The numerical computation is very demanding in the vicinity of the phase transition due to the diverging correlation length. This translates into a numerical error in the critical temperature indicated by the error bars in the plots. Figures 4 and 5 show the up- and down-quark condensates for different values of eB. The inverse magnetic catalysis effect described in Refs. [48,49] is evident. While the chiral condensate still rises with the external field

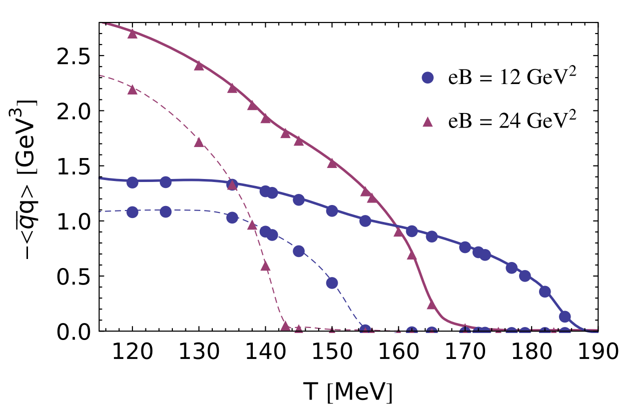

FIG. 4 (color online). Comparison of the chiral condensate (scenario 1) for up (continuous lines) and down quarks (dashed lines) at $eB = 12\ \mathrm{GeV}^2$ and $eB = 24\ \mathrm{GeV}^2$.

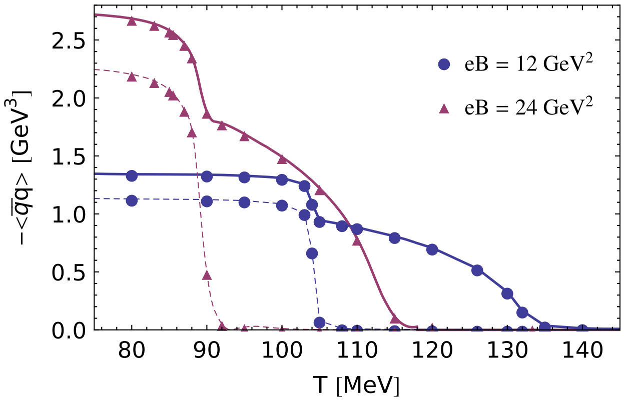

FIG. 5 (color online). Comparison of the chiral condensate for scenario 2 at $eB = 12\ \mathrm{GeV}^2$ and $eB = 24\ \mathrm{GeV}^2$.

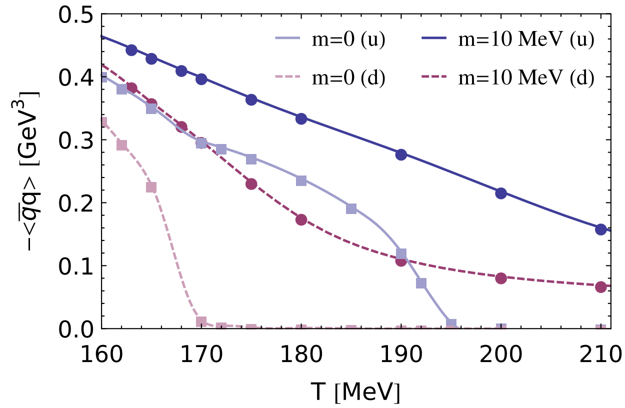

FIG. 6 (color online). Comparison of the chiral condensate at zero bare mass and at a finite bare quark mass of $m_u = m_d = 10$ MeV at $eB = 4\ \mathrm{GeV}^2$ in scenario 1.

in the low-temperature limit, the transition between chiral broken and symmetric phase drops. This signals inverse magnetic catalysis, as observed on the lattice [47,48]. Furthermore, the phase transition, which is second order at zero magnetic field, turns into a crossover with growing eB, even for vanishing bare quark masses. This can be understood as magnetic screening: the magnetic field effectively serves as an infrared cutoff, which inhibits an infinite correlation length.

In the present computation in two-flavor QCD, an even more intricate effect is observed. Up and down quarks come with different electric charges; therefore the presence of a strong electromagnetic field breaks isospin explicitly. This results in a nondegenerate chiral phase transition for the two flavors. Because gluons travel through a medium filled with both virtual up and down quarks, isospin breaking affects the self-interactions of the quarks, which leads to interference between the chiral transitions of the two flavors as seen in Figs. 4 and 5.

This interference can be interpreted as follows: Virtual quark fluctuations contributing to the gluon screening are suppressed in the chiral broken phase by the quark mass. Since the down quark undergoes the chiral phase transition already at lower scales, its fluctuations are suddenly enhanced due to the vanishing mass in the symmetric phase. The up quark, while still in its chirally broken phase, is drastically affected by these enhanced fluctuations, which lead to reduction of the up-quark condensate even below the real phase transition.

It can be seen from Figs. 4 and 5 that this effect is more prominent in scenario 2, which should come as no surprise, as the coupling of the magnetic field to the gauge sector is probably overestimated here. Nevertheless, the isospin induced chiral transition substructure is observable in the limiting scenario 1 as well, which is a strong indication of its validity. Therefore, this important physical effect might be observable in lattice calculations, as well. In Refs. [48,49] the averaged chiral condensate was investigated at finite quark mass. However, when we investigate the chiral transition at a bare quark mass of 10 MeV, we find that the interference effect is completely masked by the crossover behavior, as can be seen in Fig. 6. Note that here the unregularized condensate at finite bare mass is plotted, hence the offset between the curves.

In analogy with lattice calculation, we define T_c at the inflection points of the curves shown. In Figs. 7 and 8, the obtained values for T_c for the limiting cases described by scenarios 1 and 2 are shown. The two curves give lower and upper limits for T_c, as discussed before. The chiral transition temperature is decreasing for a large range in eB before it seems to saturate for intermediate values in both scenarios. With very large fields it rises again.

In accordance with our previous discussions, we see that the up- and down-quark chiral transitions do not coincide. The transition temperature from the flavor-averaged quark condensate is given in Figs. 7 and 8 as well. As can be seen from Figs. 4 and 5, the transition temperature of the flavor-averaged condensate is essentially determined by the up quark.

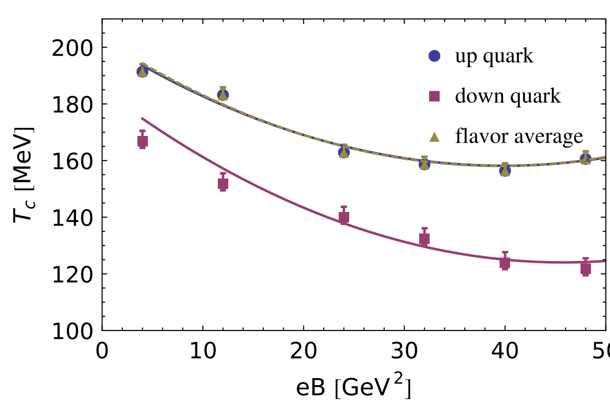

FIG. 7 (color online). Critical temperature obtained from scenario 1 for the up quark, for the down quark, and from the flavor-averaged condensate.

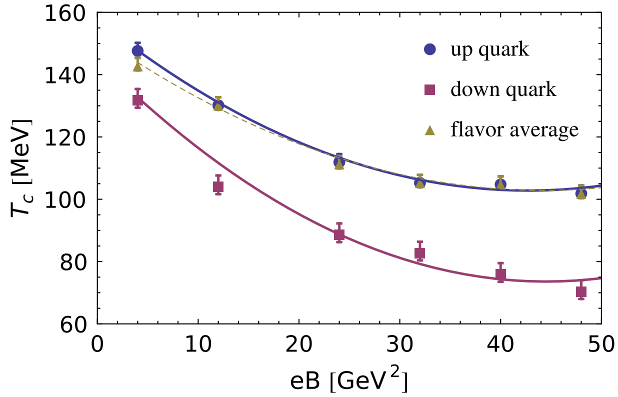

FIG. 8 (color online). Critical temperature obtained from scenario 2.

Both scenarios give estimates for the chiral transition temperature, which differ only quantitatively. Scenario 1, which underestimates the magnetic field effects in the gluon sector, extrapolates to a critical temperature at $eB = 0$ between 170 and 210 MeV with a turning point between catalysis and inverse catalysis of about $eB \approx 30\ \mathrm{GeV}^2$. On the other hand, scenario 2 gives a T_c at zero magnetic field of about 140 to 165 MeV with a turning point slightly higher than in scenario 1. This is in accordance with the fact that scenario 2 overestimates the gluonic sector, which is the source of the inverse catalysis effects. At $B = 0$, the chiral phase transitions for up and down quarks coincide. While the continuous lines in Figs. 7 and 8 are obtained from a fit with a simple quadratic polynomial, reflecting the turnover behavior at large fields, these should not be mistaken as extrapolations towards zero. Furthermore, the computations have been performed in the lowest Landau-level approximation. This leads to an uncertainty of about 10% for B smaller than $10\ \mathrm{GeV}^2$, while the qualitative behavior is not affected, as discussed in Refs. [6,8]. In the following section, we will see that the behavior of T_c at small B is steeper than just quadratic.

It is well known that within approximation schemes such as the one discussed here, relative fluctuation scales are usually well accounted for, whereas absolute scales have to be fixed. The position of T_c at $eB = 0$ gives us the possibility of identifying absolute scales and allows us to adjust our truncation. We will not be concerned about matching the exact scale of T_c at zero magnetic field with the lattice; moreover, we will investigate the mechanisms behind the $B - T$ phase structure in greater detail. We will discuss the issue of scales in the following sections.

III. ANALYTIC APPROACHES

In the present section, we are specifically interested in the mechanisms at work in magnetic and inverse magnetic catalysis. To that end we discuss approximations to the quark gap equation in Sec. III A, as well as to the dynamics of the four-Fermi coupling or quark scattering kernel in Sec. III B, that allow for an analytic approach to chiral symmetry breaking. While the quark gap equation can be straightforwardly reduced to an analytic form from that used for the numerical study, the four-Fermi coupling is studied in a renormalization group approach to QCD that reduces to an NJL-type model for low momentum scales.

A. Quark gap equation

The mechanisms behind the phenomena observed in our numerical study can be analyzed within approximations detailed below that allow for an analytic access. These approximations to the gap equation have been introduced in Ref. [13] for QED, and can be extended to QCD at finite temperature. The self-consistent DSE equation for the mass functions reads in the lowest Landau-level approximation with zero bare mass

$$M(p_\parallel) = 4\pi C_F \sum\!\!\!\!\!\!\int_{q_\parallel} \frac{M(q_\parallel)\mathrm{Tr}(\Delta(\mathrm{sgn}(eB))\gamma_\parallel^\mu\gamma_\parallel^\nu)}{M^2(q_\parallel)+q_\parallel^2} \times \int_{k_\perp} \alpha_s \exp\left(-\frac{k_\perp^2}{2|eB|}\right)\frac{P_{\mu\nu}(k)}{k^2+\Pi(k^2)}. \tag{10}$$

Here $\sum\!\!\!\!\!\!\int = T\sum_n \int \mathrm{d}q_\parallel/(2\pi)^3$ and $\Delta(s) = (1+s\sigma^3)/2$. The quark gap equation (10) is obtained from a skeleton expansion of the effective action, e.g. Ref. [80], and is nothing but a manifestly renormalization-group-invariant approximation of the above DSE equations; see the discussion in Sec. II B. It includes only dressed vertices. In Appendix A, we discuss how the interaction kernels can be related in both pictures. The 1PI quark-gluon vertex is parametrized as

$$\Gamma^\mu_{\bar{q}Aq}(q^2) = Z_A^{1/2}(q^2)\sqrt{4\pi\alpha_s(q^2)}\gamma_\parallel^\mu. \tag{11}$$

The gluon propagator is transversal due to the Landau gauge, and we allow for a gluonic mass via thermal and magnetic effects. $M(p_\parallel)$ is a function that is approximately constant in the IR but falls off rapidly for $p_\parallel^2 \geq 2|eB|$. Hence, if we are interested in $M(0) = M_{\mathrm{IR}}$, we can write, dividing the equation by its trivial solution,

$$1 - 4\pi^2 C_F T \sum\!\!\!\!\!\!\int_{q_\parallel}^{2eB} \frac{1}{M_{\mathrm{IR}}^2 + q_{\parallel,f}^2} \times \int \mathrm{d}x \frac{\alpha_s \exp(-x/2|eB|)}{q_{\parallel,b}^2 + x + \Pi(x, q_{\parallel,b})}\left(2 - \frac{q_{\parallel,b}^2}{q_{\parallel,b}^2 + x}\right) = 0. \tag{12}$$

In (12) we have introduced $q_{\parallel,b} \equiv (q_3, 2n\pi T)$ and $q_{\parallel,f} \equiv (q_3, 2\pi T(n+1/2))$. Chiral symmetry breaking is realized once a solution $M_{\rm IR}^2 > 0$ exists. Due to the shape of $M(q)$ and the exponential factor in (12), the integrand only has support for $x \lesssim 2|eB|$. In the following, we carefully investigate the ingredients to this self-consistent equation and the physical mechanisms which are responsible for the intriguing behavior seen in the previous section.

Due to the finite support of the integrand, the momenta running through the vertices are comparable to or smaller than the relevant dimensionful quantities eB and T^2. Note that in our numerical study we have used an ansatz for the quark-gluon vertex that includes generic eB and T dependencies. Here we utilize the fact that the running of α_s is dominated by the temperature and magnetic field scales. We resort to a simple ansatz for $\alpha_s(Q^2/\Lambda_{\rm QCD}^2)$ based on the analytic coupling $\alpha_{s,\rm HQ}$ suggested in Refs. [81,82]; see Ref. [83] for an investigation within the present context. This coupling yields a linear potential such as seen in the heavy quark limit:

$$\alpha_s(z) = \alpha_{s,\rm HQ}(z) r_{\rm IR}(z), \tag{13}$$

where

$$\alpha_{s,\rm HQ}(z) = \frac{1}{\beta_0}\frac{z^2-1}{z^2\log(z^2)}, \tag{14}$$

with $\beta_0 = (33-2N_f)/12\pi$ and

$$z^2 = \frac{\lambda_B 2eB + \lambda_T(2\pi T)^2}{\Lambda_{\rm QCD}^2}, \tag{15}$$

with coefficients λ_T, λ_B, which are of order 1. These coefficients determine the point at which eB or T dominate momentum scales. For the relevant magnetic fields and temperatures, the running of the coupling with temperature is very small compared to the running with eB. We use an ansatz for the infrared behavior of the vertex, which is parametrized in $r_{\rm IR}$. Here we use

$$r_{\rm IR}(z^2) = \frac{z^4}{(z^2+b^2)^2}\left(1+\frac{c^2}{z^2+b^2}\right), \tag{16}$$

which scales with $\propto z^4$ for $z\to 0$, and approaches unity in the perturbative regime. Equation (13) reproduces the correct behavior of the full quark gluon vertex in (11). We leave b and c as parameters which allow us to model the infrared behavior of the quark-gluon vertex. Our ansatz for (16) is motivated from the quantitative renormalization group study of quenched QCD in Ref. [75], which we use to determine b and c. We get

$$b = 1.50, \qquad c = 7.68 \tag{17}$$

from the fit to Fig. 4 in Ref. [75].

Furthermore, we discuss the gluon self-energy in the presence of magnetic fields at finite temperature in this simplified setup. It is important to notice that we can facilitate our calculations by the following argument: The function on the right-hand side of (12) is a continuous real function of $M_{\rm IR}$ and approaches $+1$ as $M_{\rm IR}\to\infty$. Hence, it is sufficient to check whether the expression is negative for $M_{\rm IR}=0$, because then it had to pass through zero at some point, which means that a solution exists.

The gluon self-energy receives two important contributions. The first is through the appearance of fermion loops, which are also present in an Abelian calculation. The fermionic self-energy part in lowest Landau-level approximation with $M_{\rm IR}=0$ factorizes

$$\Pi_f^{\mu\nu}(p) = \alpha eB \exp(-p_\perp^2/2eB)\Pi^{\mu\nu}(p_\parallel, T). \tag{18}$$

Contracting with $P^{\mu\nu}$ in the Landau gauge, we can write the second term as

$$\begin{aligned}\Pi_f(p_\parallel, T) &\\ &= -8\pi^2[3-2(1-p_\parallel^2/p^2)]\frac{1}{\tau^2}\\ &\quad\times\int_0^1 \mathrm{d}x \sum\!\!\!\!\!\!\!\int_{\tilde q_\parallel} \frac{x(x-1)}{(\tilde q_3^2+(2\pi)^2(n+1/2)^2+x(1-x)/\tau^2)^2},\end{aligned} \tag{19}$$

where we define $\tau^2\equiv T^2/p_\parallel^2$. The function can be evaluated numerically and is very well described by the simple function

$$\Pi_f(p_\parallel, T) = (1/2\pi)[3-2(1-p_\parallel^2/p^2)]\frac{1}{1+(4\pi^2/3)\tau^2}. \tag{20}$$

Equations (18) and (20) state that the relevant contributions to the self-energy stem from $p_\perp^2\approx 2eB$ and $p_\parallel^2\approx T^2$. Similarly to before, the influence of the magnetic field on the Yang-Mills sector is not easily accounted for. Here we focus on the Abelian-like part of the gluon self-energy. As we have investigated before numerically, this is qualitatively correct, and we will use Eq. (15) to account for the correct scales. It is well known from DSE studies [84] that approximations similar to this semi-bare-vertex ansatz underestimate the strength of chiral symmetry breaking, due to the negligence of important tensor structures in the vertex, especially those structures that break chiral symmetry explicitly [75]. In order to compensate for the overall weakness of the interaction, we allow for a phenomenological parameter κ in front of the integral in Eq. (12).

Using our simple ansatz we can investigate chiral symmetry. In Fig. 9 a family of solutions to Eq. (12) is

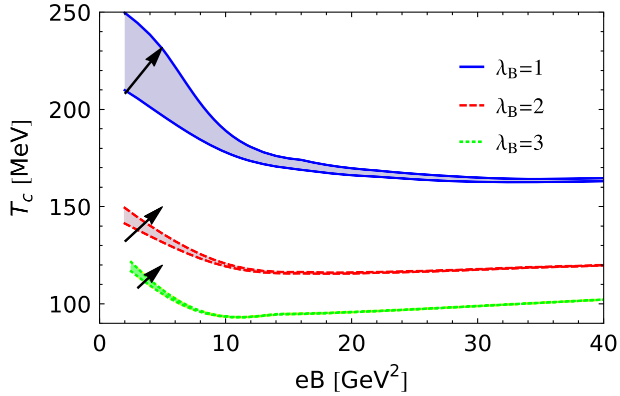

FIG. 9 (color online). Analytic calculation of the critical temperature for the chiral phase transition. The bands indicated correspond to $\lambda_T = 1$ and $\lambda_T = 0$. Arrows indicate the direction from $\lambda_T = 1$ to $\lambda_T = 0$.

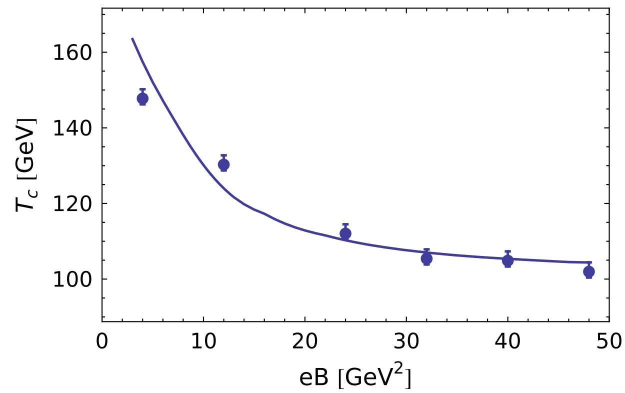

FIG. 10 (color online). Comparison of the critical temperature obtained with our full numerical procedure to the simple analytic estimate for $\lambda_B = 1.1$, $\lambda_T = 1$ and $\kappa = 1.19$.

shown for various values of λ_B and λ_T, using the ansatz described above with $\kappa = 1.2$ for the two upper curves and $\kappa = 1.4$ for the lower curves. The choice of κ is for better visualization only, as the curves can be shifted up and down using this parameter.

The observed behavior agrees with that in our numerical study. It can be seen from Fig. 9 that for small eB inverse magnetic catalysis is present, while at large eB the critical temperature rises again with the magnetic field, with

$$T_c(B/\Lambda_{\mathrm{QCD}}^2 \to \infty) \propto \sqrt{eB}, \tag{21}$$

as one would anticipate from dimensional considerations. This behavior is universal for all λ_B and λ_T. We see that the choice of λ_B affects the position of the turning point of the chiral phase boundary.

With the present analytical considerations, the numerical results in Figs. 7 and 8 are readily explained: they roughly correspond to $\lambda_B \approx 1$, which explains the relatively large value of eB at the turning point. We see that already small changes in λ_B have a huge effect on this quantity; see Fig. 9.

In Fig. 10, we have plotted the analytic result with $\lambda_B = 1.1$, $\lambda_T = 1$ and $\kappa = 1.19$, which agrees well with the numerical results from scenario 2. Based on the present work we estimate that $\lambda_B \approx 2 - 3$ is a realistic choice for the B dependence of the running coupling, as in our numerical study the quark and gluon propagators turn into their corresponding $B = 0$ propagators at this momentum scale.

The present analysis reveals the following mechanism: The gauge sector acquires a B dependence through the feedback of the fermionic sector. This dependence is responsible for the phenomenon called inverse magnetic catalysis, as has also been observed recently in a FRG study within QCD [43]. This also explains why it cannot be seen in model calculation without explicit QCD input. From Eqs. (12), (13) and (20), we see that the gluon screening and the running of the strong coupling (by both thermal and magnetic effects) are competing with the generic fermionic enhancement of chiral symmetry breaking in a dimensionally reduced system. We see from Fig. 9 that for small magnetic fields, screening effects dominate the behavior of the fermionic self-energy, while for asymptotically large fields, thermal fluctuations are negligible, and hence eB, as the dominating scale, drives the phase transition towards higher T_c (magnetic catalysis).

B. Four-Fermi coupling

For a further analytical grip, we also resort to a low-energy effective theory point of view: integrating out the gapped gluons leads to an effective four-Fermi theory that is initialized at about the decoupling scale of the glue sector of $\Lambda \approx 1$ GeV. Previously there have been phenomenological approaches in low-energy effective models to include QCD dynamics as the source of the inverse magnetic catalysis effect [24,25,55]. From the point of view of the FRG for QCD, this can be seen as follows [60,70,74,75,85–87]: At a large momentum scale k QCD is perturbative, and the 1PI effective action Γ_k in (8) is well described perturbatively. A four-Fermi coupling is generated from the one-loop diagrams (in full propagators and vertices) encoded in (8); the related diagrams are depicted in Fig. 11. In the present discussion we have dropped diagrams that depend on the $q\bar{q} - AA$ vertex, the $qq\bar{q}\,\bar{q} - AA$ vertex and the $qqq\bar{q}\,\bar{q}\,\bar{q}$ vertex. Furthermore, we assume a classical tensor structure for the $\bar{q}Aq$ vertex with a coupling $\sqrt{4\pi\alpha_{s,k}}$ and only consider the scalar-pseudoscalar four-Fermi vertex

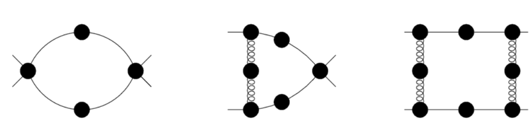

FIG. 11. Diagrams contributing to the renormalization group flow of the four-Fermi coupling.

$$\Gamma_{\text{four-Fermi}}[q,\bar{q},B] = \frac{1}{2}\bar{q}_i^{a\alpha} q_j^{b\alpha} \Gamma^{abcd}_{k,ijlm} \bar{q}_l^{c\beta} q_m^{d\beta}, \quad (22)$$

with the scalar-pseudoscalar tensor structure

$$\Gamma^{abcd}_{k,ijlm} = \lambda_k[\delta_{ij}\delta_{lm}\delta^{ab}\delta^{cd} + (\mathrm{i}\gamma_5)_{ij}(\mathrm{i}\gamma_5)_{lm}(\tau^n)^{ab}(\tau^n)^{cd}]. \quad (23)$$

The four-Fermi term in (22) can be viewed as the interaction term of a NJL-type model. Within the approximation to QCD outlined above, the flow of the four-Fermi coupling, $\partial_t\lambda_k$, has the form

$$\partial_t\lambda_k = -k^2\lambda_k^2 F_\lambda(G_q) - \lambda_k\alpha_{s,k}F_{\lambda\alpha_s}(G_q,G_A) - \frac{\alpha_{s,k}^2}{k^2}F_{\alpha_s^2}(G_q,G_A), \quad (24)$$

with positive coefficients F_λ, $F_{\lambda\alpha_s}$, F_{α_s}. The respective diagrams are depicted in Fig. 11. The different classes of diagrams in Fig. 11 depend on combinations of gluon and quark propagators G_A and G_q, respectively.

The four-Fermi coupling λ_k in two-flavor QCD at $T=0$ has been quantitatively computed (including its momentum dependence) in quenched QCD with the FRG in Ref. [75], and in a more qualitative approximation (without its momentum dependence) in fully dynamical QCD in Ref. [74]. The respective results are depicted in Fig. 12. As expected, the couplings have a similar dependence and maximal strength. However, the slope of the coupling in the qualitative computation in the peak regime relevant for chiral symmetry breaking is bigger for the qualitative computation. This can be traced back to the missing momentum dependencies, whose lack artificially increases the locality in momentum space and in the cutoff scale. Hence, guided by the experience gained in the DSE computations, we expect the slope to play a large role, and we shall use the quantitative quenched results for λ_k and α_s in our present computations. We shall further comment on the differences in the next section.

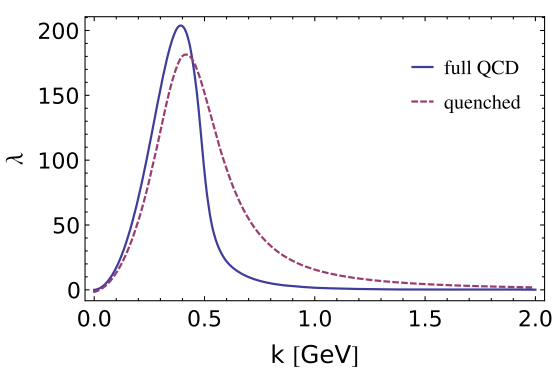

FIG. 12 (color online). Scalar-pseudoscalar four-Fermi coupling in the vacuum, $T=0$, $B=0$, computed with quantitatively reliable QCD flows in quenched QCD [75], and with qualitative full QCD flows [74].

For large cutoff scales k, the propagators approach the classical propagators. The current quark mass at these scales is negligible, and only the cutoff scale is present if temperature and magnetic field are considered small relative to the cutoff scale. Then the dimensionless F's are simple combinatorial factors. For optimized regulators [88], they are given as

$$F_\lambda = 4N_c, \qquad F_{\lambda\alpha_s} = 12\frac{N_c^2-1}{2N_c}, \quad F_{\alpha_s^2} = \frac{3}{16}\frac{9N_c^2-24}{N_c} \quad (25)$$

in the vacuum; see e.g. Refs. [74,75,87] for more details. For small enough cutoff scales k, the gluonic diagrams decouple due to the QCD mass gap. In the Landau gauge this can be directly seen with the gapping of the gluon propagator. For $T=0$, $B=0$, this entails

$$p^2 G_A(p^2 \lesssim \Lambda^2) \propto p^2/m_{\text{gap}}^2, \quad (26)$$

with $\Lambda \approx 1$ GeV. We emphasize that (26) only reflects the mass gap present in the Landau gauge gluon propagator; the gluon propagator is not that of a massive particle; see e.g. Ref. [89]. For momentum scales $p^2 \lesssim \Lambda^2$, this approximately leaves us with an NJL-type model with the action

$$\Gamma_{\text{NJL}}[q,\bar{q},B] = \int_x \bar{q}\mathrm{i}\partial q + \Gamma_{\text{four-Fermi}}[q,\bar{q},B], \quad (27)$$

with the scalar-pseudoscalar four-Fermi interaction defined in (22). In the presence of a magnetic field, this model including fermionic fluctuations has been investigated in Ref. [38] within the FRG. Here we shall use the respective results within the lowest Landau-level approximation. Then T_c shows an exponential dependence on the dimensionful parameter eB:

$$T_c = 0.42\Lambda \exp\left(-\frac{2\pi^2}{N_c\lambda_\Lambda \sum_f |q_f eB|}\right). \quad (28)$$

The well-known exponential dependence of T_c on the four-Fermi coupling λ_Λ already explains the large sensitivity of the scales of magnetic catalysis and inverse magnetic catalysis to details of the computation. Equation (28) is valid for large magnetic fields and for $\Lambda \ll m_{\text{gap}}^2$—that is, deep in the decoupling regime of the gluons. An estimate that also interpolates to small magnetic fields is given by

$$T_c = 0.42\Lambda \exp\left(-\frac{1}{c_\Lambda\lambda_\Lambda}\right), \quad (29)$$

with

$$c_k(B) = \frac{N_c}{2\pi^2}\left(\sum_f |q_f eB| + c_1 k^2\right), \quad \text{with} \quad c_1 = 3, \tag{30}$$

where c_1 has been adjusted to reproduce $T_c(B=0) \approx 158$ MeV. While Eq. (30) resembles a lowest-Landau-level approximation, it is actually an expansion in B. Using this ansatz, we can describe the behavior of the phase transition on scales below 1 GeV^2 qualitatively, while the $B = 0$ limit is fixed.

It is also well known that for $k \gg m_{\mathrm{gap}}$ the flow of the four-Fermi coupling is driven by the gluonic diagrams summed up in F_{α_s}: for large scales we can set $\lambda_{k\gg m_{\mathrm{gap}}} \approx 0$. The gauge coupling is small, $\alpha_{s,k\gg m_{\mathrm{gap}}} \ll 1$, and the flow gives $\lambda_k \propto \alpha_s^2$. This entails that the diagrams with four-Fermi couplings are suppressed by additional powers of α_s, and the four-Fermi coupling obeys

$$\partial_t \lambda_{\mathrm{glue},k} = -\frac{\alpha_{s,k}^2}{k^2} F_{\alpha_s}(G_q, G_A), \tag{31}$$

where the subscript "glue" indicates that the flow is driven by glue fluctuations. As discussed before, for $k \gg m_{\mathrm{gap}}$ we have classical dispersions for quarks and gluons, and the diagrammatic factor F_{α_s} is a constant; see (25). The strong coupling $\alpha_{s,k}$ has the form (13) with $z \propto k$. Integrating (31) with (13) gives

$$\lambda_{\mathrm{glue},k} \propto \frac{\alpha_{s,k}^2}{2k^2} F_{\alpha_s}(G_q, G_A), \tag{32}$$

where an estimate for the B dependence of the gluonic diagram in F_{α_s} is given in Appendix B.

At vanishing magnetic field, $\lambda_{\mathrm{glue},k}$ agrees well with the full result for the four-Fermi coupling in Ref. [75] for $k \gtrsim 2$ GeV; see Fig. 13. Below $k \approx 2$ GeV, $\lambda_{\mathrm{glue},k}$ is increasingly smaller than the full scalar-pseudoscalar four-Fermi coupling in quenched QCD. In this intermediate range, where all diagrams contribute, we write the resulting coupling within a resummed form that captures already the fermionic diagram proportional to F_λ,

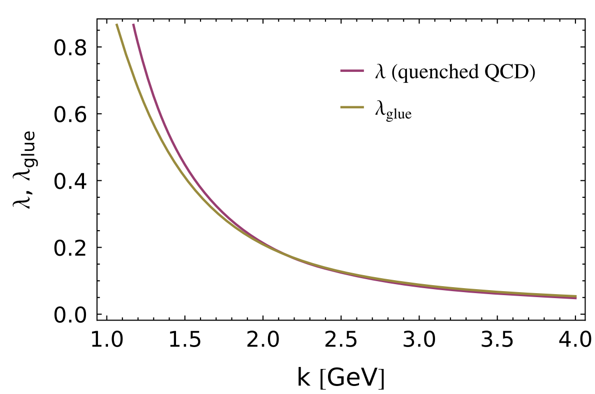

FIG. 13 (color online). Scalar-pseudoscalar four-Fermi coupling at $T = 0$, $B = 0$, computed with quantitatively reliable QCD flows in quenched QCD [75], in comparison to λ_{glue} computed from (32).

$$\lambda_k = \frac{\bar\lambda_k}{1 - \bar c_k \bar\lambda_k}, \quad \text{with} \quad \bar c_k = \int_k^\Lambda dk' k' F_\lambda(G_q). \tag{33}$$

The resummed form in (33) already reflects the matter part of the flow in (24), which is the term proportional to $\partial_t \lambda_k$. The other terms add up to

$$\partial_t \bar\lambda_k = -(1 - \bar c_k \bar\lambda_k)^2 \left(\lambda_k \alpha_{s,k} F_{\lambda\alpha_s} + \frac{\alpha_{s,k}^2}{k^2}\right). \tag{34}$$

For $\bar c_k \bar\lambda_k \ll 1$, the flow of $\bar\lambda_k$ boils down to (31). For $\bar c_k \bar\lambda \to 1$, the flow in (34) tends towards zero. In this regime the four-Fermi coupling grows large and the matter flow dominates. Hence, for the present qualitative analysis we simply identify $\bar\lambda$ with the glue λ_{glue}, (32), up to a prefactor,

$$\bar\lambda_k = Z_\lambda \lambda_{\mathrm{glue},k}. \tag{35}$$

The prefactor Z_λ accounts for the fact that we have used results of quantitative QCD flows [75] for the strong coupling which also include wave function renormalizations for the quarks. In the current model considerations without wave function renormalization and further simplifications, this has to be accounted for. For the same reason, the normalization 0.42Λ related to a four-Fermi flow with an optimized regulator has to be generalized. Moreover, the prefactor $\bar c_{\lambda,k}$ is the integrated four-Fermi flow already present in (29) up to an overall normalization accounting for the model simplifications. We choose

$$\bar c_k(B) = c_3 c_k(B) \quad \text{and} \quad 0.42\Lambda \to 0.42\Lambda \exp(c_2 - c_3) \tag{36}$$

and arrive at

$$T_c = 0.42\Lambda \exp\left(-\frac{1}{c_\Lambda \bar\lambda_\Lambda} + c_2\right), \tag{37}$$

with c_Λ as given in (30) and $\bar\lambda$ in (35) and (32). Note that the parameter c_3 has dropped out. Its value can be adjusted to achieve a quantitative agreement of (32) with the QCD result in Ref. [75] with

$$c_3 = \frac{1}{2Z_\lambda}, \tag{38}$$

where the factor $1/Z_\lambda$ simply removes the mapping factor adjusting for the missing wave function renormalizations in the model computation. This quantitative agreement

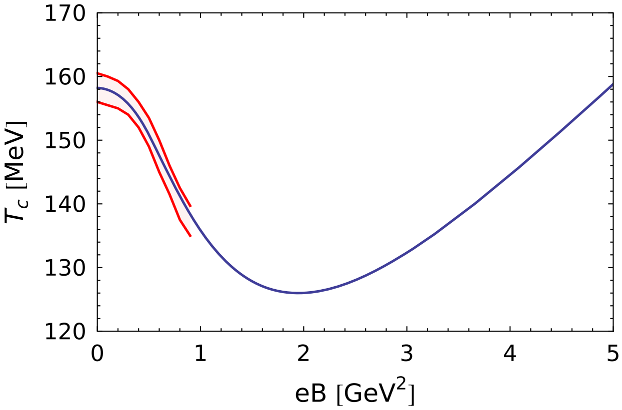

FIG. 14 (color online). Comparison of the chiral transition temperature obtained within the simple mean field NJL estimate in Eq. (14) to the lattice results of Ref. [47] (see their Fig. 10).

strongly supports the reliability of the approximate solution to the flow equation given by (33) in the intermediate momentum regime that is of importance for the current considerations. The remaining parameters are fixed as follows:

$$Z_\lambda = 2.2, \qquad c_1 = 3, \qquad c_2 = 1.4. \tag{39}$$

The parameter c_1 has already been adjusted to meet $T_c(B=0) \approx 158$ MeV; see (29) and (30). The parameter c_2 readjusts the overall scale $0.42\Lambda \to 0.42\Lambda \exp c_2 = 1.7\Lambda$. As already discussed above, it depends on the regulator and the approximation at hand. It reflects the dependence on the renormalization group scheme. Similarly to c_1, it is fixed with $T_c(B=0) \approx 158$ MeV and is a function of the overall normalization of the four-Fermi coupling Z_λ. The latter is the only free parameter left. In (39) we use the value that reproduces the lattice results; see Fig. 14. We emphasize that no other parameter is present that allows us to shift the minimum in T_c, the latter being a prediction.

Obviously, the effect seen in our numerical and analytic DSE study is also present in the analytic approach to the dynamics of the four-Fermi coupling, including a direct grip on the underlying mechanisms. We see that the nonmonotonous behavior, i.e. the delayed magnetic catalysis [43,52], is already present at smaller scales compared to Figs. 7 and 8, while the lattice results are reproduced.

In turn, for asymptotically large magnetic fields, the critical temperature runs logarithmically with B:

$$T_c(B/\Lambda_{\mathrm{QCD}}^2 \to \infty) \propto \ln B/\Lambda_{\mathrm{QCD}}, \tag{40}$$

related to a double-log dependence on B of the exponent. Due to the qualitative nature of the approximation of the B dependence of the gluon propagator, it cannot be trusted for asymptotically large B. Indeed, (40) has to be compared to (21) within the analytic DSE approach predicting a square-root dependence. Note that in the latter computation, the quark vacuum polarization is included self-consistently at large B even though the backreaction on the pure glue loops in Fig. 2 is neglected. Still, this indicates the validity of the square-root dependence, even though a definite answer to this question requires more work.

C. Discussion of scales and mechanisms

With the findings of the last two sections, we have achieved an analytic understanding of the mechanisms at work. The decrease of T_c for small magnetic fields, the increase of T_c for larger fields, as well as the related magnetic field regimes can now be understood. In particular, this concerns the magnetic field B_{min}, where $T_c(B_{\mathrm{min}})$ is at its minimum. This is the turning point between increasing and decreasing $T_c(B)$.

Magnetic catalysis relates to the dimensional reduction due to the magnetic field in diagrams with quark correlation functions leading to an increase of the condensate. At finite temperature, the catalysis due to the dimensional reduction is accompanied by a thermal gapping of the quarks that counteracts against the magnetic catalysis effects. In total, this leads to a rise of both the chiral condensate and the critical temperature, if the magnetic field dependence of the involved couplings is sufficiently small. As the magnetic field also sets a momentum scale of the physics involved, this scenario holds true for sufficiently large magnetic field strength $eB/\Lambda_{\mathrm{QCD}}^2 \gg 1$, where the B dependence of the couplings can be computed (semi)perturbatively. This explains the regime of delayed magnetic catalysis.

The above discussion of the standard scenario already entails that rapidly changing couplings are required for a decreasing T_c. The couplings involved are the scalar-pseudoscalar four-Fermi coupling λ_k and the strong coupling $\alpha_{s,k}$, where k sets the momentum scale. Both are rising rapidly towards the infrared for momentum scales $k \lesssim 4-10$ GeV; for λ_k, see Fig. 13. In this regime, chiral symmetry breaking and confinement is triggered and takes place in QCD at vanishing magnetic field. Switching on the magnetic field increases the relevant momentum scale $k^2 \propto eB$, and hence decreases λ and α_s. The condensate still grows with B, as the B enhancement in the broken phase is still present; only T_c decreases.

Our results from the analytic approach to the quark gap equation, presented in Fig. 9, support these findings. The position of the turning point B_{min} in both the full numerical as well as the analytic analysis of the gap equation depends crucially on the magnetic field and temperature dependence of the quark-gluon vertex; see Fig. 9. When contrasted with the quantitative FRG results of α_s in Ref. [75], the strong coupling in (A2) decays considerably more slowly towards the UV. In turn, the couplings in the qualitative FRG study for full QCD [74] have a steeper decay; for the four-Fermi coupling see Fig. 13. Seemingly, this already explains the large value of B_{min} in the current DSE study as well as the small value of B_{min} in Ref. [43], which uses approximations similar to Ref. [74]. Note, however, that we have used the quenched quantitative α_s in the analytic DSE study which agrees well with the numerical DSE result for $\lambda_B \approx 1$.

In summary, we have identified the physics mechanisms behind the $T-B$ phase diagram from our full QCD calculations. Moreover, Fig. 14 suggests a turning point for $eB_{\min} \approx 1.5-10\ \mathrm{GeV}^2$, the large regime for $eB_{\min}$ being related to the exponential dependence on the couplings. Evidently, the effects observed depend on a sensitive balance of different scales and parameters. Hence, further studies are required to fully uncover the intricate underlying dynamics. Very recent findings in AdS/QCD models [36] indicate an inverse magnetic catalysis behavior up to $eB \approx 4\ \mathrm{GeV}^2$, which supports our findings.

IV. CONCLUSIONS

We have investigated the chiral phase structure of QCD at finite temperature in the presence of an external magnetic field. Our study resolves the discrepancy between recent lattice and continuum calculations at magnetic fields below $1\ \mathrm{GeV}^2$; see also Ref. [43]. We confirm the inverse magnetic catalysis effect seen in lattice studies at small B. At larger B we see that magnetic catalysis is restored, with $T_c \propto \sqrt{eB}$. Indications for the turnover behavior have already been found in Ref. [43], and in Ref. [52] within two-color lattice QCD. We hope that further lattice calculations in full QCD at the scales discussed here will become feasible soon.

The reason for this nonmonotonous behavior is screening effects of the gauge sector, i.e. modifications of the gluon self-energy, as well as the strong coupling α_s in the presence of magnetic fields. Moreover, we have investigated the nature of the chiral transition for a finite magnetic field.

Apart from the B dependence of the critical temperature, we observe that the phase transition in the chiral limit turns smoothly into a crossover with rising B. Notably, we find a nondegeneracy in the phase transition which is due to the explicit isospin breaking caused by the different electric charges of up and down quarks. This nondegeneracy might lead to phenomenological consequences in experimental studies of the QCD phase diagram with noncentral heavy-ion collisions, as there might be a mixed phase between the up and down quark transitions. Recent lattice calculations [90] support the possibility of a nondegenerate chiral phase transition.

In addition, our calculations show that, due to this isospin breaking, there is a steplike behavior in the up quark condensate triggered by the chiral transition of the down quark. While this is an significant effect in the chiral limit, it smoothens out rapidly with increasing current quark mass. Physical current quark masses are in the transition regime, and this effect might have phenomenological consequences. To our knowledge, this is a novel effect in the QCD phase diagram, and it certainly deserves further investigation.

We have used analytic studies of the quark gap equation and the dynamics of the four-Fermi coupling for an investigation of the physics mechanisms behind (inverse) magnetic catalysis. The results are discussed at length in the previous Sec. III C, leading to a rough prediction of the turning point at $eB_{\min} \approx 1.5-10$ GeV. Our investigations highlight the rich phenomenology of QCD matter in external magnetic fields, which motivates further studies, e.g. at finite chemical potential, towards more realistic descriptions of matter under extreme conditions. Recent studies [91] have suggested even richer QCD phase structures in the presence of magnetic fields.

ACKNOWLEDGMENTS

We thank J. Braun, C. S. Fischer, K. Fukushima, W. A. Mian, M. Mitter, S. Rechenberger, F. Rennecke, and N. Strodthoff for discussions and work on related subjects. This work is supported by the Helmholtz Alliance HA216/EMMI and Grant No. ERC-AdG-290623. N. M. acknowledges support by the Studienstiftung des Deutschen Volkes.

APPENDIX A: GLUON PROPAGATOR AND QUARK-GLUON VERTEX FROM DYSON-SCHWINGER STUDIES

Here we discuss the truncation scheme for the quark gap equation and the gluon propagator, based on Refs. [71,79]. The quark-gluon vertex is taken as $\Gamma^\mu = z_{qgq}\gamma^\mu$, with

$$z_{qgq}(Q^2) = \frac{d_1}{d_2 + Q^2} \tag{A1}$$

$$+ \frac{Q^2}{\Lambda^2 + Q^2}\left(\frac{\beta_0 \alpha(\mu) \log Q^2/\Lambda^2 + 1}{4\pi}\right)^{2\delta}, \tag{A2}$$

containing the parameters

$$d_1 = 7.9\ \mathrm{GeV}^2, \qquad d_2 = 0.5\ \mathrm{GeV}^2,$$
$$\delta = -18/88, \qquad \Lambda = 1.4\ \mathrm{GeV}. \tag{A3}$$

Here the scales must be identified correctly in order to capture the correct dependence with T and eB. We take Q to be the symmetric momentum $Q^2 = (q^2 + p^2 + (q-p)^2)/3$ at the vertex with $Q^2 = Q_3^2 + Q_0^2 + Q_\perp^2$, where $Q_0^2 = (2\pi T)^2$ if $Q_0^2 < (2\pi T)^2$ and $Q_\perp^2 = 2|eB|$ if $Q_\perp^2 < 2|eB|$. We note that this roughly corresponds to an identification of scales as in Sec. III A with $\lambda_B \approx 1$, although the present vertex is clearly more sophisticated, as it includes momentum dependencies and thereby generic eB effects. For a current overview of the quark-gluon vertex in DSE truncations, see Refs. [92,93]. Furthermore, in order to be able to solve the gluon DSE equation, we rely on lattice input for the Yang-Mills part, which we then "dress" with magnetic field effects, as described above. The reliability of this truncation was already discussed in detail at finite temperature [71] and utilized in the presence of magnetic fields before [6]. The lattice fit is given by

$$Z_{\mathrm{YM}}^{-1}(Q^2) = \frac{Q^2\Lambda^2}{(Q^2+\Lambda^2)^2}\left[\left(\frac{c}{Q^2+a\Lambda^2}\right)^b + \frac{Q^2}{\Lambda^2}\left(\frac{\beta_0\alpha(\mu)\log Q^2/\Lambda^2+1}{4\pi}\right)^\gamma\right], \quad \text{(A4)}$$

with

$$\Lambda = 1.4\ \mathrm{GeV}, \qquad c = 11.5\ \mathrm{GeV}^2, \qquad \beta_0 = 11N_c/3, \qquad \gamma = -13/22, \quad \text{(A5)}$$

where $\alpha(\mu) = 0.3$ and a and b are temperature-dependent parameters, which can be found in Ref. [79]. As discussed before, the DSE truncation scheme can be related to the skeleton expansion done in our analytic estimate, which was motivated by renormalization group invariance:

$$4\pi\alpha_s(Q^2)r_{\mathrm{IR}}(Q^2)\frac{P_{\mu\nu}}{Q'^2+\Pi} \equiv \frac{P_{\mu\nu}}{Z_{\mathrm{YM}}Q'^2+\Pi_f}z_{qgq}, \quad \text{(A6)}$$

where the sum over different polarization tensor components is implied. The right-hand side actually serves as the input to our numerical study, while the different components of Π are determined dynamically from solving the gluon DSE equation.

APPENDIX B: MAGNETIC FIELD DEPENDENCE OF THE FOUR-FERMI COUPLING FROM QCD

As we have discussed in Sec. III B, the value of the NJL coupling λ at the intrinsic cutoff scale of the model is determined by QCD dynamics. At large scales, the dynamics of λ is driven by the rightmost diagram shown in Fig. 11. Within simplifications, we will motivate the functional dependence of this diagram on temperature and the magnetic field. In the lowest Landau-level approximation, the quarks are constrained to the t-z plane denoted by $(\|)$, whereas the gluons propagate in all four dimensions $(\|,\perp)$. We write the gluon box diagram in Fig. 11 at zero external momentum as

$$F_{\alpha_s}(eB \geq 0.3\ \mathrm{GeV}) \simeq 4.5eB\int_0^\infty dq_\|, \frac{q_\|}{q_\|^2+m_q^2+\alpha_s eBc_q}\int_0^\infty dq_\perp, \frac{q_\perp}{[q_\perp^2+q_\|^2+m_A^2+eB\alpha_s c_A]^2}, \quad \text{(B1)}$$

where α_s is given as Eq. (13).

For $eB < 0.3$, (B1) is smoothly (quadratic fit) extrapolated to $eB = 0$, minimizing the eB dependence. The flavor, color and Dirac tensor indices have been contracted, and the comparison with the results for λ in quenched QCD shown in Fig. 13 shows that the prefactor resulting from the tensor contract is approximately 4.5. We have written the propagators in a semiperturbative form with medium-dependent mass terms. Further, we have taken $m_A \approx 1$ GeV as the decoupling scale; $m_q \approx 300$ MeV in the chiral broken phase and $c_A = c_q = 1$. Strictly speaking, both masses are larger than 1 GeV, as we have to add the cutoff masses $\propto \Lambda^2$. We have chosen smaller masses in order to also potentially have access to the infrared domain $k \to 0$, where the constituent quark mass is of the order 0.3 GeV and the gluonic mass gap is of the order 1 GeV. Furthermore, we have approximated the Matsubara sum by an integration, due to the small level spacing compared to the magnetic field. This approximation does not hold for small eB, but (B1) is only used for $eB \geq 0.3$ GeV. Equation (B1) includes the correct dependence on α_s as well and thus captures eB and T effects qualitatively. The model parameters in Sec. III B allow us to reproduce the quantitative behavior of the chiral transition temperature, and a more elaborate version of Eq. (B1) does not give much greater insight. Apart from the agreement with the T_c results from lattice calculation, Fig. 13 shows that quantitatively reliable results from QCD-flows in quenched QCD [75] are reproduced.

[1] I. A. Shovkovy, Lect. Notes Phys. **871**, 13 (2013).
[2] M. D'Elia, Lect. Notes Phys. **871**, 181 (2013).
[3] K. Fukushima, Lect. Notes Phys. **871**, 241 (2013).
[4] D. E. Kharzeev, L. D. McLerran, and H. J. Warringa, Nucl. Phys. **A803**, 227 (2008).
[5] K. Fukushima, D. E. Kharzeev, and H. J. Warringa, Phys. Rev. D **78**, 074033 (2008).
[6] N. Mueller, J. A. Bonnet, and C. S. Fischer, Phys. Rev. D **89**, 094023 (2014).
[7] J. O. Andersen, W. R. Naylor, and A. Tranberg, arXiv:1411.7176.
[8] V. A. Miransky and I. A. Shovkovy, Phys. Rep. **576**, 1 (2015).
[9] G. Basar, D. Kharzeev, and V. Skokov, Phys. Rev. Lett. **109**, 202303 (2012).

[10] G. Basar, D. E. Kharzeev, and E. V. Shuryak, Phys. Rev. C **90**, 014905 (2014).
[11] V. Gusynin, V. Miransky, and I. Shovkovy, Nucl. Phys. **B462**, 249 (1996).
[12] V. Gusynin, V. Miransky, and I. Shovkovy, Phys. Rev. Lett. **83**, 1291 (1999).
[13] V. Gusynin, V. Miransky, and I. Shovkovy, Nucl. Phys. **B563**, 361 (1999).
[14] V. Gusynin, V. Miransky, and I. Shovkovy, Phys. Rev. D **52**, 4747 (1995).
[15] T. Inagaki, D. Kimura, and T. Murata, Prog. Theor. Phys. **111**, 371 (2004).
[16] J. K. Boomsma and D. Boer, Phys. Rev. D **81**, 074005 (2010).
[17] M. D'Elia, S. Mukherjee, and F. Sanfilippo, Phys. Rev. D **82**, 051501 (2010).
[18] A. J. Mizher, M. Chernodub, and E. S. Fraga, Phys. Rev. D **82**, 105016 (2010).
[19] R. Gatto and M. Ruggieri, Phys. Rev. D **82**, 054027 (2010).
[20] R. Gatto and M. Ruggieri, Phys. Rev. D **83**, 034016 (2011).
[21] B. Chatterjee, H. Mishra, and A. Mishra, Phys. Rev. D **84**, 014016 (2011).
[22] R. Gatto and M. Ruggieri, Lect. Notes Phys. **871**, 87 (2013).
[23] M. Frasca and M. Ruggieri, Phys. Rev. D **83**, 094024 (2011).
[24] M. Ferreira, P. Costa, O. Lourenco, T. Frederico, and C. Providencia, Phys. Rev. D **89**, 116011 (2014).
[25] E. Ferrer, V. de la Incera, and X. Wen, Phys. Rev. D **91**, 054006 (2015).
[26] R. Farias, K. Gomes, G. Krein, and M. Pinto, Phys. Rev. C **90**, 025203 (2014).
[27] A. Ayala, M. Loewe, A. J. Mizher, and R. Zamora, Phys. Rev. D **90**, 036001 (2014).
[28] A. Ayala, M. Loewe, and R. Zamora, Phys. Rev. D **91**, 016002 (2015).
[29] L. Yu, J. Van Doorsselaere, and M. Huang, Phys. Rev. D **91**, 074011 (2015).
[30] O. Bergman, G. Lifschytz, and M. Lippert, J. High Energy Phys. 05 (2008) 007.
[31] C. V. Johnson and A. Kundu, J. High Energy Phys. 12 (2008) 053.
[32] V. G. Filev, C. V. Johnson, and J. P. Shock, J. High Energy Phys. 08 (2009) 013.
[33] F. Preis, A. Rebhan, and A. Schmitt, J. High Energy Phys. 03 (2011) 033.
[34] F. Preis, A. Rebhan, and A. Schmitt, Lect. Notes Phys. **871**, 51 (2013).
[35] A. Ballon-Bayona, J. High Energy Phys. 11 (2013) 168.
[36] K. A. Mamo, J. High Energy Phys. 05 (2015) 121.
[37] V. Skokov, Phys. Rev. D **85**, 034026 (2012).
[38] K. Fukushima and J. M. Pawlowski, Phys. Rev. D **86**, 076013 (2012).
[39] K. Kamikado and T. Kanazawa, J. High Energy Phys. 03 (2014) 009.
[40] K. Kamikado and T. Kanazawa, J. High Energy Phys. 05 (2015) 121.
[41] J. O. Andersen and A. Tranberg, J. High Energy Phys. 08 (2012) 002.
[42] J. O. Andersen, W. R. Naylor, and A. Tranberg, J. High Energy Phys. 04 (2014) 187.
[43] J. Braun, W. A. Mian, and S. Rechenberger, arXiv:1412.6025.
[44] T. Kojo and N. Su, Phys. Lett. B **720**, 192 (2013).
[45] T. Kojo and N. Su, Phys. Lett. B **726**, 839 (2013).
[46] P. Watson and H. Reinhardt, Phys. Rev. D **89**, 045008 (2014).
[47] G. S. Bali, F. Bruckmann, G. Endrődi, Z. Fodor, S. D. Katz, S. Krieg, A. Schäfer, and K. K. Szabó , J. High Energy Phys. 02 (2012) 044.
[48] G. S. Bali, F. Bruckmann, G. Endrődi, Z. Fodor, S. D. Katz, and A. Schäfer , Phys. Rev. D **86**, 071502 (2012).
[49] G. S. Bali, F. Bruckmann, G. Endrodi, F. Gruber, and A. Schäfer, J. High Energy Phys. 04 (2013) 130.
[50] F. Bruckmann, G. Endrodi, and T. G. Kovacs, J. High Energy Phys. 04 (2013) 112.
[51] G. S. Bali, F. Bruckmann, G. Endrodi, S. D. Katz, and A. Schäfer, J. High Energy Phys. 08 (2014) 177.
[52] E. M. Ilgenfritz, M. Muller-Preussker, B. Petersson, and A. Schreiber, Phys. Rev. D **89**, 054512 (2014).
[53] V. Bornyakov, P. Buividovich, N. Cundy, O. Kochetkov, and A. Schaefer, Phys. Rev. D **90**, 034501 (2014).
[54] K. Fukushima and Y. Hidaka, Phys. Rev. Lett. **110**, 031601 (2013).
[55] E. Fraga, B. Mintz, and J. Schaffner-Bielich, Phys. Lett. B **731**, 154 (2014).
[56] J. O. Andersen, W. R. Naylor, and A. Tranberg, J. High Energy Phys. 02 (2015) 042.
[57] J. M. Pawlowski, AIP Conf. Proc. **1343**, 75 (2011).
[58] L. M. Haas, R. Stiele, J. Braun, J. M. Pawlowski, and J. Schaffner-Bielich, Phys. Rev. D **87**, 076004 (2013).
[59] T. K. Herbst, M. Mitter, J. M. Pawlowski, B.-J. Schaefer, and R. Stiele, Phys. Lett. B **731**, 248 (2014).
[60] J. M. Pawlowski, Nucl. Phys. **A931**, 113 (2014).
[61] D. Lee, C. N. Leung, and Y. Ng, Phys. Rev. D **55**, 6504 (1997).
[62] V. Miransky and I. Shovkovy, Phys. Rev. D **66**, 045006 (2002).
[63] C. N. Leung and S.-Y. Wang, Ann. Phys. (Amsterdam) **322**, 701 (2007).
[64] A. Ayala, A. Bashir, A. Raya, and E. Rojas, Phys. Rev. D **73**, 105009 (2006).
[65] E. Rojas, A. Ayala, A. Bashir, and A. Raya, Phys. Rev. D **77**, 093004 (2008).
[66] V. Ritus, Ann. Phys. (N.Y.) **69**, 555 (1972).
[67] V. Ritus, Sov. Phys. JETP **48**, 788 (1978).
[68] C. S. Fischer, P. Watson, and W. Cassing, Phys. Rev. D **72**, 094025 (2005).
[69] D. Nickel, R. Alkofer, and J. Wambach, Phys. Rev. D **74**, 114015 (2006).
[70] J. Braun, L. M. Haas, F. Marhauser, and J. M. Pawlowski, Phys. Rev. Lett. **106**, 022002 (2011).
[71] C. S. Fischer and J. Luecker, Phys. Lett. B **718**, 1036 (2013).
[72] C. S. Fischer, L. Fister, J. Luecker, and J. M. Pawlowski, Phys. Lett. B **732**, 273 (2014).
[73] C. S. Fischer, J. Luecker, and C. A. Welzbacher, Phys. Rev. D **90**, 034022 (2014).
[74] J. Braun, L. Fister, J. M. Pawlowski, and F. Rennecke, arXiv:1412.1045.
[75] M. Mitter, J. M. Pawlowski, and N. Strodthoff, Phys. Rev. D **91**, 054035 (2015).

[76] C. N. Leung and S.-Y. Wang, Nucl. Phys. B**747**, 266 (2006).
[77] T.-K. Chyi, C.-W. Hwang, W. Kao, G.-L. Lin, K.-W. Ng, and J.-J. Tseng, Phys. Rev. D **62**, 105014 (2000).
[78] J. M. Pawlowski, Ann. Phys. (Amsterdam) **322**, 2831 (2007).
[79] C. S. Fischer, A. Maas, and J. A. Muller, Eur. Phys. J. C **68**, 165 (2010).
[80] C. S. Fischer and J. M. Pawlowski, Phys. Rev. D **80**, 025023 (2009).
[81] A. Nesterenko, Phys. Rev. D **62**, 094028 (2000).
[82] A. Nesterenko, Phys. Rev. D **64**, 116009 (2001).
[83] N. Christiansen, M. Haas, J. M. Pawlowski, and N. Strodthoff, arXiv:1411.7986.
[84] R. Alkofer, C. S. Fischer, F. J. Llanes-Estrada, and K. Schwenzer, Ann. Phys. (Amsterdam) **324**, 106 (2009).
[85] J. Braun and H. Gies, J. High Energy Phys. 06 (2006) 024.
[86] J. Braun and H. Gies, Phys. Lett. B **645**, 53 (2007).
[87] J. Braun, J. Phys. G **39**, 033001 (2012).
[88] D. F. Litim, Phys. Lett. B **486**, 92 (2000).
[89] C. S. Fischer, A. Maas, and J. M. Pawlowski, Ann. Phys. (Amsterdam) **324**, 2408 (2009).
[90] G. Endrodi, arXiv:1504.08280.
[91] K. Nishiyama, S. Karasawa, and T. Tatsumi, arXiv:1505.01928.
[92] R. Alkofer, G. Eichmann, C. S. Fischer, M. Hopfer, M. Vujinovic *et al.*, *Proc. Sci. QCD-TNT-III* (2013) 003.
[93] R. Williams, Eur. Phys. J. A **51**, 57 (2015).